Deep Learning-Driven Simultaneous Layout Decomposition and Mask Optimization

Wei Zhong, Shuxiang Hu, Yuzhe Ma, *Member, IEEE*, Haoyu Yang, Xiuyuan Ma, and Bei Yu, *Member, IEEE*

***Abstract*—Combining multiple patterning lithography (MPL) and optical proximity correction (OPC) pushes the limit of 193-nm wavelength lithography to go further. Considering that layout decomposition may generate plenty of solutions with diverse printabilities, relying on conventional mask optimization (MO) process to select the best candidate for manufacturing is computationally expensive. Therefore, an accurate and efficient printability estimation is crucial and can significantly accelerate the layout decomposition and MO (LDMO) flow. In this article, we propose a convolutional neural network (CNN)-based prediction and integrate it into our new high-performance LDMO framework. The optimization process can be considerably improved as the decomposition quality has been inferred in the early phase. To facilitate the network training and ensure better estimation accuracy, we develop sampling strategies for both layout and decomposition. Moreover, we enhance the layout sampling approach by adopting autoencoder to distance evaluation that promises superior sampling results. The experimental results demonstrate the effectiveness and the efficiency of the proposed algorithms.**

***Index Terms*—Convolutional neural network, Design for manufacturing, layout decomposition, mask optimization.**

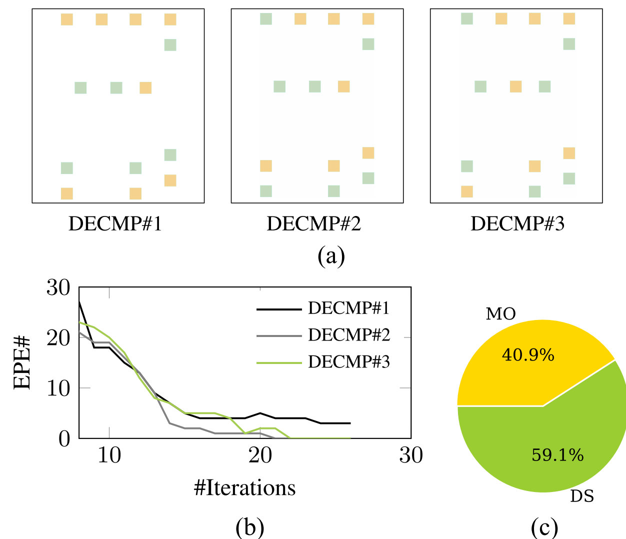

Fig. 1. Optimization runtime and decomposition convergence comparison. (a) Different decomposition optimization results of the same layout. (b) Corresponding decomposition convergence of EPE. (c) Runtime breakdown: Comparison between DS and MO.

I. Introduction

The SHRINKAGE of device feature size has reached the resolution limit of the 193-nm wavelength lithography, thus various resolution enhancement techniques (RETs) are heavily applied to maintain a good printability when transferring patterns from mask to wafer, among which multiple patterning lithography (MPL) and optical proximity correction (OPC) are two very promising approaches.

MPL is currently widely applied to enhance the resolution in the industry. The key step in litho-etch-litho-etch (LELE)-type MPL is the layout decomposition which assigns the conflicting patterns on a layer to separated masks for manufacturing. To achieve better decomposition quality, various methods have been proposed [1]–[4]. OPC or mask optimization (MO) is able to handle the optical distortions in subwavelength lithography by refining the pattern shapes on a mask. Various inverse lithography technology (ILT)-based approaches are proposed to implement the OPC process [5]–[8].

After decomposing a layout, multiple solutions can be obtained, as shown in Fig. 1 (a). To further enhance the printability, MO is performed. Since the MO is a subsequent step of the layout decomposition, the final quality is determined, to a large extent, by the layout decomposition result. Fig. 1 (b) shows corresponding trajectories during MO of different decomposition results. It is observed that the printability is not consistently good or bad for a given instance. Only after the entire process is completed can we tell the good ones from the bad ones. However, it is computationally expensive to run all solutions through the MO process due to the overhead imposed by lithography modeling. Recently it has been demonstrated that a simultaneous layout decomposition and MO (LDMO) framework can ease the gap and obtain high printability masks in a unified way [9], in which the final masks are generated by the collaboration of MO engine and

Manuscript received June 13, 2020; revised September 17, 2020 and December 9, 2020; accepted February 10, 2021. Date of publication February 23, 2021; date of current version February 21, 2022. This work was supported in part by the National Natural Science Foundation of China (NSFC) under Grant 61906029; in part by the Fundamental Research Funds for the Central Universities; and in part by the Research Grants Council of Hong Kong SAR under Grant CUHK24209017. The preliminary version has been presented at the ACM/IEEE Design Automation Conference (DAC) in 2020. This article was recommended by Associate Editor X. L. Behjat.
(Corresponding authors: Wei Zhong; Bei Yu.)

Wei Zhong, Shuxiang Hu, and Xiuyuan Ma are with the DUT-RU International School of Information Science and Engineering, Dalian University of Technology, Dalian 116024, China, and also with the Key Laboratory for Ubiquitous Network and Service Software of Liaoning Province, Dalian 116024, China.

Yuzhe Ma, Haoyu Yang, and Bei Yu are with the Department of Computer Science and Engineering, Chinese University of Hong Kong, Hong Kong SAR, China.

Digital Object Identifier 10.1109/TCAD.2021.3061494

1937-4151 © 2021 IEEE. Personal use is permitted, but republication/redistribution requires IEEE permission.
See https://www.ieee.org/publications/rights/index.html for more information.

Authorized licensed use limited to: The Hong Kong University of Science and Technology (Guangzhou). Downloaded on December 20,2024 at 09:27:14 UTC from IEEE Xplore. Restrictions apply.

discrete optimization engine. However, given a situation like Fig. 1 (b), the method proposed in [9] is not an ideal solution. On one hand, leveraging MO engine for printability estimation is expensive as mentioned before. Fig. 1 (c) shows the proportion of MO and decomposition selection (DS) of [9]. It can be seen that DS even takes more than 50% to find a proper decomposition, which motivates us to explore a more efficient way for DS, i.e., printability estimation. On the other hand, the greedy pruning is based on the printability of intermediate MO results, which is not an accurate estimation and hence leads to suboptimal solutions. Therefore, an efficient and accurate printability prediction approach is of importance to enhance and accelerate the design flow.

Deep learning has drawn great attention for its ability to learn automatically from a large amount of data. Compared with the traditional feature extraction methods, learning features from training data is more suitable to characterize the rich internal information of the data. In the electronic design automation (EDA) field, deep learning has been widely applied in various EDA applications. As the most conventional model, convolutional neural networks (CNNs) have been adopted for routability estimation [10], lithography hotspot detection [11], and resist modeling [12]. However, deep learning is far from a perfect method for printability estimation. In order to achieve higher estimation accuracy, a large amount of labeled data is usually the bottleneck due to the following two reasons.

1) The decomposition quality is labeled by OPC, which is an extremely time-consuming optimization process and hence restricts the amount of training data.
2) The distribution of training data also determines the generalization of the trained model. Unbalanced layout diversity in the training set introduces difficulties for training. Therefore, we have to cluster layouts to sample training data.

An important problem for clustering layouts is defining the distance between two layouts. In the image processing field, scale-invariant feature transform (SIFT) [13] is a widely applied algorithm that outputs a set of key points that are detected from different scales of Difference-of-Gaussian (DOG) images. These key points describe local features and are invariant to scaling and rotation. Since the excellent performance in practice, they are adopted to many complex tasks, such as facial recognition [14] and forgery detection [15]. Therefore, taking SIFT points as the reference of layout similarity evaluation is a promising solution.

In this work, we propose a deep learning-driven framework to predict and further improve the printability of masks. The framework contains a layout decomposition generation module, a printability estimation module and a MO module. To obtain high-quality decomposition candidates, we build no-odd graphs to address conflicts. Due to the exponentially growing solution space, enumerating all possible pattern combinations is not applicable. Instead, n-wise method is applied to generate representative decomposition candidates. Since we can hardly evaluate the printability of a decomposition result by formulating the physical rules, CNN is used to help us select the best decomposition candidate. Besides, in order to promote the accuracy of prediction and accelerate the training process, we design layout distance metrics based on SIFT and autoencoder to cluster similar layouts, and sample instances from each cluster. Considering the large complexity of OPC limits the size of the training set, the decomposition sampling approach also uses n-wise method to obtain training-friendly decomposition results. The main contributions of this work are as follows.

1) We propose a CNN predictor to estimate the printability before optimizing masks.
2) We combine the no-odd graph and n-wise method to generate layout decomposition candidates more efficiently.
3) We develop a set of sampling approaches to select the representative decomposition as the training set. The comparison with random sampling strategy shows the superiority of our sampling method.
4) We improve the sampling strategy by integrating autoencoder into our training flow to ensure better layout similarity evaluation.
5) Experimental results show that our framework outperforms other previous works and reduces edge placement error (EPE) by 81.9% in comparison with state-of-the-art methods.

The remainder of this article is organized as follows. Section II introduces the background of double patterning lithography and gives the problem definition. Section III describes the optimization framework. Section IV shows the details of training the prediction module, including layout sampling, decomposition sampling, and CNN training steps. Experimental results are detailed in Section V. Sections VI and VII, respectively, present the discussion for future work and conclusion.

TABLE I
NOTATIONS IN THIS ARTICLE

Notation	Description
$\boldsymbol{T}'$	Target image
$\boldsymbol{T}_i$	The printed image of the i-th mask
$\boldsymbol{M}_i$	The i-th mask
$\boldsymbol{I}_i$	The i-th aerial image
$\boldsymbol{I}_{th}$	The threshold of constant photo-resist model
$\boldsymbol{h}_k$	The k-th convolution kernel
$\otimes$	Matrix convolution

II. PRELIMINARIES

Notations and their descriptions in this article are listed in Table I.

The task of MO for double patterning lithography is to generate a pair of optimized masks such that the final printed image $\boldsymbol{T}$ and the target image $\boldsymbol{T}'$ are as close as possible. The lithography simulation process can be represented by two models: 1) optical model and 2) photo-resist model.

The theoretical basis of optical model is the Hopkins diffraction model [16] which has been widely applied to a partially coherent imaging system. It is given by

$$\boldsymbol{I}_i(x, y) = \sum_{k=1}^{N^2} w_k \cdot |\boldsymbol{M}_i(x, y) \otimes \boldsymbol{h}_k(x, y)|^2 \tag{1}$$

where $\boldsymbol{M}_i$ is a given mask to calculate the aerial image $\boldsymbol{I}_i$. $\boldsymbol{h}_k$ is the kth optical kernel, w_k is the weight of $\boldsymbol{h}_k$. The system contains N^2 illumination sources in total.

Due to the high complexity of the Hopkins diffraction model, a singular value decomposition (SVD) method [17]

Authorized licensed use limited to: The Hong Kong University of Science and Technology (Guangzhou). Downloaded on December 20,2024 at 09:27:14 UTC from IEEE Xplore. Restrictions apply.

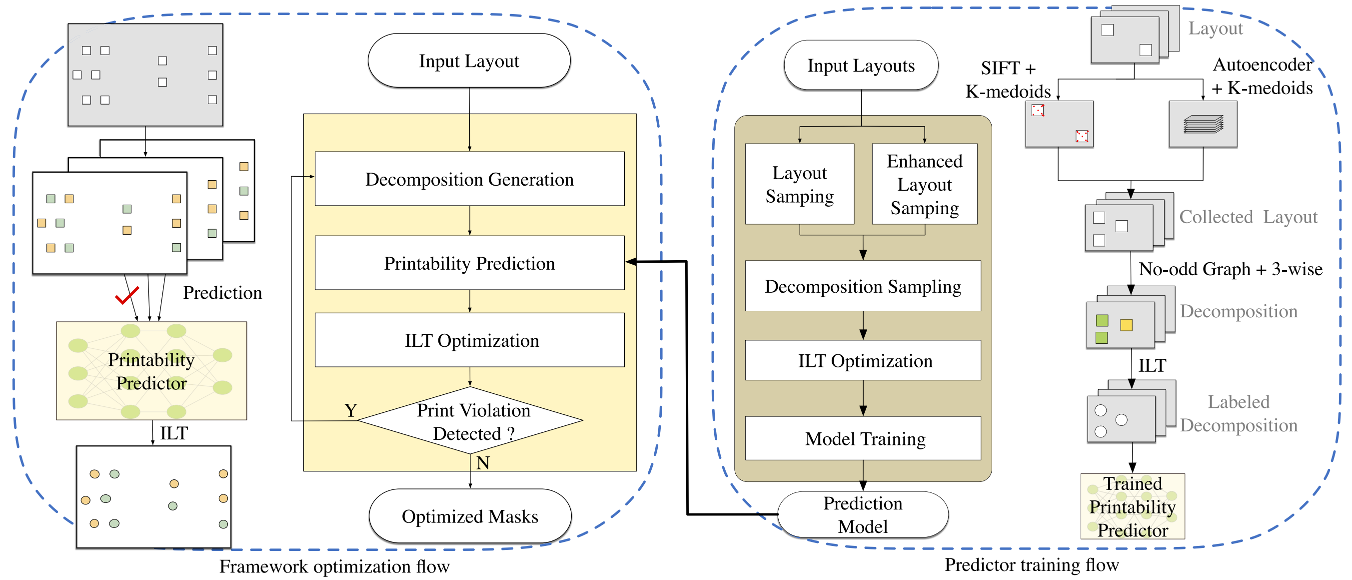

Fig. 2. Overall flow.

is adopted for approximation, which is described as

$$\boldsymbol{I}_i(x, y) \approx \sum_{k=1}^{K} w_k \cdot |\boldsymbol{M}_i(x, y) \otimes \boldsymbol{h}_k(x, y)|^2 \tag{2}$$

where K is the total kernel number we selected to approximate the optical system.

The photo-resist model controls the printing of final wafer image. The shape is printed to the final image, when the intensity is greater than a given threshold, as shown in

$$\boldsymbol{T}_i(x, y) = \begin{cases} 1, & \text{if } \boldsymbol{I_i}(x, y) \geq I_{\text{th}} \\ 0, & \text{if } \boldsymbol{I_i}(x, y) < I_{\text{th}}. \end{cases} \tag{3}$$

In order to use ILT to optimize masks, a new variable $\boldsymbol{P}_i$ is introduced and the sigmoid function [18] is applied to binary value $\boldsymbol{M}_i$ so that they are differentiable, as expressed in

$$\boldsymbol{M}_i(x, y) = \frac{1}{1 + e^{-\theta_m \boldsymbol{P}_i(x,y)}}. \tag{4}$$

In this way, the binary mask $\boldsymbol{M}$ is expressed with unbound parameter $\boldsymbol{P}$. θ_m is the coefficient to control the slope of the sigmoid function. Similarly, the relaxed photo-resist model can be presented as

$$\boldsymbol{T}_i(x, y) = \frac{1}{1 + e^{-\theta_t(\boldsymbol{I}_i(x,y) - \boldsymbol{I}_{\text{th}})}}. \tag{5}$$

In our implementation, hyperparameters θ_m, θ_t are set to 8, 120 to achieve better optimization performance. I_{th} is set to 0.039 according to [19]. In double patterning ILT, the printed image is organized in the following form:

$$\boldsymbol{T}(x, y) = \min\{\boldsymbol{T}_1(x, y) + \boldsymbol{T}_2(x, y), 1\}. \tag{6}$$

Then we can derive the gradient of $\boldsymbol{T}(x, y)$ with respect to $\boldsymbol{P}_i(x, y)$, and update corresponding $\boldsymbol{M}_i(x, y)$ by performing ILT to reshape masks and obtain better result $\boldsymbol{T}$. More details about the gradient formulation can be seen in [9].

Definition 1 (EPE): EPE measures the manufacturing distortion by the edge displacement between the printed image and the target layout. A checkpoint will be marked as an EPE violation if its EPE greater than a given threshold.

Definition 2 (Squared L_2 Error): Squared L_2 error measures the difference between the printed image $\boldsymbol{T}$ and the target image $\boldsymbol{T}'$, which is defined as $\|\boldsymbol{T} - \boldsymbol{T}'\|_2^2$.

EPE is one of the most important criteria of image printability. ILT process reduces the squared L_2 error in each iteration to minimize the number of EPE indirectly, and a smaller squared L_2 error indicates a better layout printability. In our work, both EPE and squared L_2 error are selected as printability metrics.

The task of layout decomposition for double patterning lithography is to generate a pair of decomposed masks so that the masks follow the design rule. This process can be presented like

$$f_{\text{decomp}}(\boldsymbol{T}') = \{\boldsymbol{M}_1, \boldsymbol{M}_2\} \tag{7}$$

where $\boldsymbol{T}'$ is the target image and $\boldsymbol{M}_1$, $\boldsymbol{M}_2$ are decomposition result. The subsequent ILT process generates optimized masks to minimize the differences between printed image and target image, (8) describes this process

$$f_{\text{ILT}}(\boldsymbol{M}_1, \boldsymbol{M}_2) = f_{\text{ILT}}(f_{\text{decomp}}(\boldsymbol{T}')) = \boldsymbol{T} \tag{8}$$

where $\boldsymbol{T}$ is the printed image after ILT optimization. We can evaluate its quality by organizing the combination form of EPE and L_2 Error. Thus, the f_{ILT} converts to a continuous function. In this work, we try to use CNN to regress the continuous function derived from (8) and use the network to supervise the process of (7) to generate a better decomposition. For simplicity and to demonstrate the methodology effectiveness, we use constant photo-resist model instead of variable threshold model. Since self-aligned double patterning (SADP) technology can be applied for metal layer, we only focus on the contact layer.

Based on the above definitions and discussions, the LDMO problem can be described as follows.

Authorized licensed use limited to: The Hong Kong University of Science and Technology (Guangzhou). Downloaded on December 20,2024 at 09:27:14 UTC from IEEE Xplore. Restrictions apply.

Problem 1 (LDMO): Given a target image $\boldsymbol{T}'$, decompose the layout to obtain mask candidates that result in fewer EPE violations upon MO.

III. Optimization Framework

The overall flow of our optimization framework is shown in Fig. 2. It contains two parts: the left part introduces the optimization flow, while the right part details the predictor training used in the printability prediction module of the left part. In this section, we focus on the framework optimization process (the left part flow). First, decomposition candidates are generated according to the input layout. In order to obtain legal decomposition candidates rapidly, we build several no-odd graphs and apply n-wise method to avoid generating violated decomposition candidates. Then all candidates are fed into the printability prediction module. The trained CNN scores each candidate and outputs the best layout decomposition. Next, ILT process is used to optimize masks and outputs the optimized final masks. Besides, print violations are checked during the ILT optimization process to avoid printability estimation errors.

A. Decomposition Generation

The decomposition generation module produces decomposed mask candidates for the next module based on the given layout. Since we are seeking for a pair of masks, $\boldsymbol{M}_1$ and $\boldsymbol{M}_2$, from these candidates to achieve the best printability, the generated candidates should contain these high-quality decomposition results. Enumerating all possible decomposition results can tackle this problem, but the time consumption is expensive even though there is a decomposition quality predictor to help select the best one. So we focus on the most promising results.

In our generating strategy, the key to generating a set of high-quality decomposed masks in the layout decomposition phase can be viewed from two different scales. In the macro view, we should solve the conflicts in accordance with the coloring rules. It ensures our decomposition results follow the design rules and discards low-quality results according to our experience. But from the perspective of micro view, coloring rules are coarse constraints we manually made, thus they can not help more in finding a hidden relationship, i.e., selecting the best decomposition among the legal decomposition candidates. Thankfully, due to the powerful modeling ability of deep networks, they are efficient in distinguishing a better result among candidates. By combining eligible decomposition results and through the use of deep networks, we are able to improve the decomposition quality further. This section mainly introduces our generating strategy, as described in Algorithm 1.

As shown in Fig. 3, layout patterns are first divided into three sets: 1) separated pattern ($\mathcal{S}_P$) set; 2) appended pattern ($\mathcal{A}_P$) set; and 3) normal pattern ($\mathcal{N}_P$) set. Based on the distance d of the nearest patterns, the belonging of pattern $\mathcal{E}$ is determined by

$$\mathcal{E} \in \begin{cases} \mathcal{S}_P, & \text{if } d \leq n_{\min} \\ \mathcal{A}_P, & \text{if } n_{\min} < d \leq n_{\max} \\ \mathcal{N}_P, & \text{if } n_{\max} < d. \end{cases} \tag{9}$$

Algorithm 1 Decomposition Generation

Require: Input layout L.
  $\mathcal{S}_P$, $\mathcal{A}_P$, $\mathcal{N}_P$ ← `PatternClassify`(L);
  V ← `SolveNoOddGraph`($\mathcal{S}_P$);
  $Arrs1$ ← `GetThreeWiseArrays`(V, $\mathcal{S}_P$, $\mathcal{A}_P$);
  $Arrs2$ ← `GetTwoWiseArrays`($\mathcal{N}_P$);
  $mergedArrs1$ ← `CheckAndMerge`($Arrs1$);
  $mergedArrs2$ ← `CheckAndMerge`($Arrs2$);
  S ← `Combine`($mergedArrs1$, $mergedArrs2$);
  for $j = 1 \to S$.`size` **do**
    K ← `DrawImage`(S_j);
    Img.`save`(K);
  end for
  return Img;

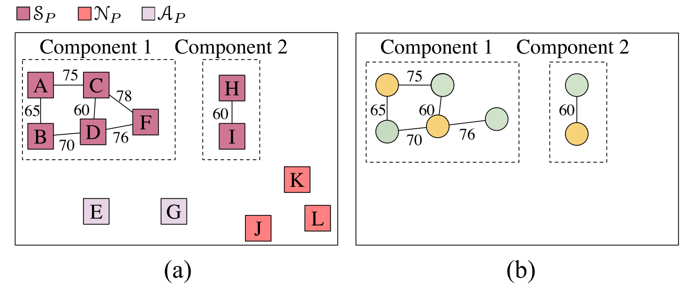

Fig. 3. $\mathcal{S}_P$ distribution solution. (a) Constructed weighted graph. (b) No-odd graph solution.

A print violation occurs when the distance between two patterns is less than $n_{\min}$, and it disappears as the distance d increases, but there may still exist the interaction between two patterns until the distance reaches $n_{\max}$. Therefore, patterns in $\mathcal{S}_P$ always cause print violations, so they ought to be separated from each other. $\mathcal{A}_P$ are the kind of patterns that tend to cause printability issues while $\mathcal{N}_P$ have minimal or no effect on the performance compared to the other two types. When generating decomposition candidates, we take different strategies according to the pattern type. In our implementation, $n_{\min}$ is set to 80 nm, and $n_{\max}$ is set to 98 nm.

We first solve the print violations in the macro view. Print violations in set $\mathcal{S}_P$ are fixed by allocating the shapes within the set to two separate masks, which is solved by constructing a weighted graph and is converted to a coloring problem. Here, we take patterns in $\mathcal{S}_p$ as vertices and the distance among them as the weight of edge, thus a weighted graph is built. But the generated weighted graph may not be a colorable graph. Therefore, in order to optimize the printability and make the generated graph colorable, our strategy is to find a min-weight graph without odd cycles for each component, which is described in Algorithm 2. For each component, we are able to obtain a weighted graph as shown in Fig. 3(a). Obviously, component 1 is not a colorable graph, so we take the component as input W, and store its edges in E. Edges in E are sorted in ascending order so that we can easily access to the edge with minimum weight by taking the first element in E. No-edge graph G is initialized according to W, which has the same vertices number, but no edges are linked. In each iteration, the first edge in E is added to G only if it does not cause

Authorized licensed use limited to: The Hong Kong University of Science and Technology (Guangzhou). Downloaded on December 20,2024 at 09:27:14 UTC from IEEE Xplore. Restrictions apply.

Algorithm 2 Build Min-Weight Graph Without Odd Cycles

Require: A weighted graph W
  Store edges of W in E;
  Sort E in an ascending order;
  Initialize a graph G without edges;
  while E is not empty **do**
    $edge \leftarrow E$.getFront();
    E.popFront();
    G.addEdge($edge$);
    if G contains odd cycles **then**;
      Delete $edge$ from G;
    end if
  end while
  return G;

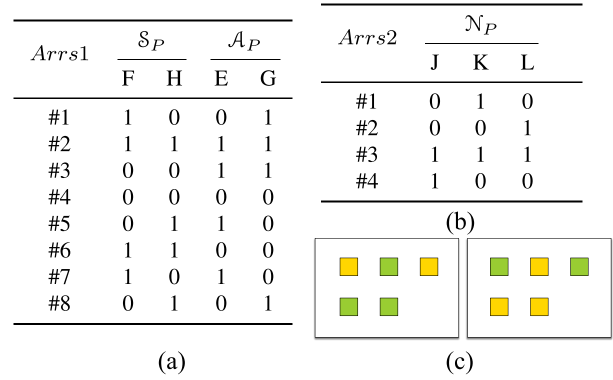

$Arrs1$	$\mathcal{S}_P$		$\mathcal{A}_P$	
	F	H	E	G
#1	1	0	0	1
#2	1	1	1	1
#3	0	0	1	1
#4	0	0	0	0
#5	0	1	1	0
#6	1	1	0	0
#7	1	0	1	0
#8	0	1	0	1

(a)

$Arrs2$	$\mathcal{N}_P$		
	J	K	L
#1	0	1	0
#2	0	0	1
#3	1	1	1
#4	1	0	0

(b)

(c)

Fig. 4. n-wise arrays and dual decomposition. (a) Generated *three*-wise arrays. (b) Generated two-wise arrays according to $\mathcal{N}_p$. (c) Two different images represent the same decomposition.

odd cycles. After handling all edges, a min-weight graph, as shown in Fig. 3(b), is prepared for coloring. Then G can be legally colored by assigning different colors to neighbor nodes. Based on the result of no-odd graph, two neighbor vertices can be assigned to different masks to avoid violations. Besides, the relative position relationship of patterns in the same no-odd graph can be inferred, which provides the basis of the following decomposition analysis.

After solving the $\mathcal{S}_P$ distribution, we consider the combination of patterns $\mathcal{A}_P$ and $\mathcal{N}_P$ in micro view. Another requirement is that we want to reduce the number of decomposition candidates as much as possible. So n-wise method is applied to generate representative decomposition candidates, meanwhile limiting the size of the candidate set. The n-wise test method (also known as combinatorial test method) has been used to test compiler by Mandl [20]. Usually, it is used to analyze the main factors affecting the experiment with the smallest test set. The main idea of n-wise method is to obtain the full factor combination of local areas at the price of giving up the global factor combination strength. Here, n represents how many factors we can test according to the generated arrays. For example, if n is 2, we can find the problem caused by the interaction of two factors.

In our decomposition process, covering all the combinations of patterns is prohibitively expensive which is similar to software testing. An example of two-wise (pairwise) arrays with four patterns is shown in

$$\begin{array}{c} \\ \text{instance \#1} \\ \text{instance \#2} \\ \text{instance \#3} \\ \text{instance \#4} \\ \text{instance \#5} \end{array} \begin{array}{c} \begin{array}{cccc} \text{factor1} & \text{factor2} & \text{factor3} & \text{factor4} \end{array} \\ \begin{bmatrix} 1 & 0 & 0 & 0 \\ 1 & 1 & 1 & 1 \\ 0 & 1 & 0 & 1 \\ 0 & 0 & 1 & 1 \\ 0 & 1 & 1 & 0 \end{bmatrix} \end{array}.$$

In the generated arrays, each row is an instance of decomposition, each column represents a pattern (factor), and the value determines which masks this pattern belongs to. Picking any two columns, the complete combination of them (00, 01, 10, 11) exists, which means two-wise method reduces the strength of factor combination to minimize the generated arrays meanwhile maintaining the complete combination of any two factors. Naturally, if n is set to the number of factors, the test set becomes Cartesian product of all factors whose size is 16. From the example we can find that the combinatorial explosion of patterns can be well handled.

Based on the no-odd graph result, we can obtain the relative position relationship of $\mathcal{S}_P$. In order to build the connection between $\mathcal{S}_P$ and $\mathcal{A}_P$, we randomly pick a pattern from each connected component as a factor and apply three-wise method together with the patterns in $\mathcal{A}_P$. Then we apply two-wise method to patterns in $\mathcal{N}_P$, thus, two arrays with different combination strengths are created. We can simply combine the arrays to get the duplicated decomposition results (some lines in the arrays actually stand for the same decomposition, we will solve this problem later). Take the layout in Fig. 3(a) as an example, there are six patterns in $\mathcal{S}_P$, two patterns in $\mathcal{A}_P$, three patterns in $\mathcal{N}_P$ and two connected components, and the corresponding no-odd graph result of the components is shown in Fig. 3(b). We randomly select pattern F in component 1 and pattern H in component 2 to apply the 3-wise method together with patterns in $\mathcal{A}_P$ (E and G), the generated $Arrs1$ can be seen in Fig. 4(a). As for patterns in $\mathcal{N}_P$ (J, K and L), two-wise method is used to generate $Arrs2$ [see Fig. 4(b)]. From Fig. 4(a) and (b), we can see that the number of instances does not grow too much with the number of factors.

We call the combination of $Arrs1$ and $Arrs2$ is duplicated decomposition results because although n-wise method generates the minimal training set of strength n, there are still identical decomposition candidates. The output of the decomposition generation module is a grayscale image with different grayscale levels to represent patterns distributed on different masks. Since the masks are unordered, a layout decomposition can be represented by two different images, as shown in Fig. 4(c). Different colors mean the patterns are distributed on different masks. To solve this problem, we number the layout patterns from left to right and from top to bottom. We manually fix the pattern numbered 1 on $\boldsymbol{M}_1$ so that the two masks become ordered. When generating the decomposition candidates, once pattern numbered 1 is distributed on $\boldsymbol{M}_2$, the value of this row will be reversed. After checking and reversing all rows, we merge the same rows to drop the same decomposition. Note that this operation will not destroy the relative position relationship among patterns. So the total decomposition candidate number should be size($mergedArrs1$) $\times$ size($mergedArrs2$).

Authorized licensed use limited to: The Hong Kong University of Science and Technology (Guangzhou). Downloaded on December 20,2024 at 09:27:14 UTC from IEEE Xplore. Restrictions apply.

B. Mask Pattern Density Balance

Layout density balance for double patterning lithography is also expected to be considered. The decomposition generation strategy in Section III-A simply combines the arrays, but it may generate imbalanced decomposition candidates. In our approach, we also designed an optional stage to balance the decomposition candidates. In *mergedArrays*1 and *mergedArrays*2, 0/1 represents which mask the pattern is distributed on. To uniformly map patterns onto two masks, the density rule checking is added before combining arrays. The checking process is implemented by counting how many 0/1 numbers in the two instances (a line in the array is called an instance), which are, respectively, from *mergedArrays*1 and *mergedArrays*2. Let P_0 denote the 0 count and P_1 is the 1 count in two instances, the balanced decomposition should obey the rule that $\frac{|P_1 - P_0|}{\max(P_1, P_0)} \leq 40\%$. The decomposition candidates are discarded if the density checking is not passed.

C. Printability Prediction

Traditional two-stage approaches focus on formulating rules to avoid violations. However, more manufacturing friendly decomposition is hardly obtained by designing the rough restrictions, i.e., build conflict graph by spacing rules, which limits the performance of further MO. The CNN can build the mapping relation from input to output, especially in the image processing field, so they are suitable for dealing with DS problems. Another advantage of CNN is that no matter what kind of searching algorithm is selected to find the best decomposition, the computationally expensive lithography simulation process will be the bottlenecks of these algorithms, but CNN replaces simulation by estimation, hence accelerates the DS process.

The printability prediction module in the left part of Fig. 2 evaluates the decomposition printability by giving candidates scores. The well-trained estimation model is obtained from the right part of Fig. 2, which shows a complete training flow and we will introduce the training process in Section IV.

In the printability prediction module, all decomposition candidates are fed to CNN in the form of grayscale images. A lower score indicates a better printability, so in order to find the best printability after the ILT optimization, this module scores each input and output the decomposition of the minimal score. Considering we have the requirement of reselecting decomposition candidates because printability prediction errors may happen, this module will cooperate with the ILT module to avoid outputting the same decomposition result. ILT module optimizes the masks meanwhile detecting print violations, and the printability prediction module gives the no-repeat decomposition. There are two measures to ensure different decomposition results.

1) Each fixed no-odd graph has two possible decomposition results, so random selecting patterns in each no-odd graph and combine the results can generate different decomposition candidates. Naturally, the selection result should vary with the given candidates.
2) The previous illegal outputs are recorded such that the printability prediction module can skip the same decomposition.

D. ILT Optimization

At this point, the best decomposition result has been obtained. This module optimizes decomposed masks meanwhile detecting print violations. Violations indicate the printability estimation error. Once they are detected, we go back to the decomposition generation step to create new decomposition candidates and use CNN to select another decomposition solution, otherwise, we continue to optimize the masks. Considering the print violations may happen at any iteration of ILT, we detect them every three iterations and the violation detection method is from the discrete optimization part of [9].

ILT process calculate the gradient g of object function $\|\boldsymbol{T} - \boldsymbol{T}'\|_2^2$ with respect to $\boldsymbol{P}_1$, $\boldsymbol{P}_2$ and update parameters in the form of $\boldsymbol{P}_i = \boldsymbol{P}_i - \text{stepSize} \times \ g$. Then, we can update $\boldsymbol{M}_i$, $\boldsymbol{I}_i$ and printed image $\boldsymbol{T}$ with new $\boldsymbol{P}_i$ according to (2)–(6). The ILT optimization will early stop when it removes all EPE violations, or it reaches the max iteration threshold. In our implementation, the iteration threshold is set to 30.

IV. Training of Prediction Network

In this section, sampling strategies and training approaches are detailed. As shown in the right part of Fig. 2, sampling strategies can be divided into two stages: 1) layout sampling and 2) decomposition sampling. We first describe the definitions of layout similarity and cluster layouts based on the distance definitions. After sampling layouts from each cluster, we introduce the decomposition sampling strategy and discuss the model structure.

A. Layout Sampling

In order to achieve the purpose of increasing layout diversity in the training set, our strategy is clustering layouts and sampling them from each cluster. The clustering method gathers similar layouts into a group, so the layouts sampled from each cluster are called representative layouts, as they have a large distance from other cluster elements. But before conducting clustering algorithms, the distance between two layouts needs to be clearly defined. Layout feature extraction has been widely investigated in recent studies. Ma [21] reflects layout distance by XOR operation. Wen *et al.* [22] used density feature vectors to extract pattern shapes. Yao *et al.* [23] encoded layout into strings to represent pattern topology. Due to the diffraction and interference of light, printed image quality is largely dependent on the nearby patterns. The distance metric should capture common layout features (e.g., recognize representative pattern distribution, ignore slight layout movement and rotation) and express light propagation property. But previous methods are not a perfect fit for our requirements.

In this section, the SIFT-based layout similarity metric is introduced, then a clustering algorithm is performed to get representative layouts.

1) SIFT Layout Distance: SIFT [13] has been widely used in computer vision field to capture local features of an image. The output of SIFT is a set of key points that are captured through a staged filtering approach [13]. The key points are detected from different scales of DOG images by searching for the extreme points, and these extreme points are filtered so that the remaining points are stable enough. The detected key points are invariant to rotation, scaling and contain the main

Authorized licensed use limited to: The Hong Kong University of Science and Technology (Guangzhou). Downloaded on December 20,2024 at 09:27:14 UTC from IEEE Xplore. Restrictions apply.

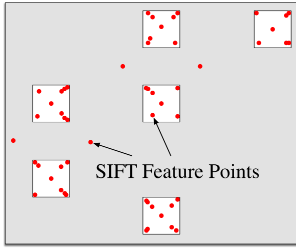

Fig. 5. Example of SIFT feature.

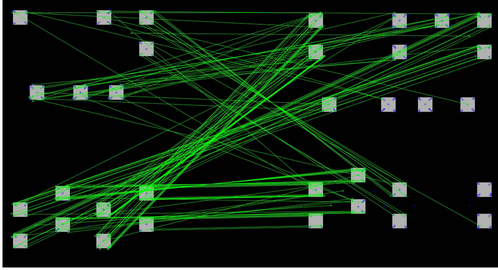

Fig. 6. Example of SIFT matching.

gradient direction, so they can be chosen as the reference for classifying the layouts. There is an example of SIFT feature point distribution in Fig. 5. The white squares are patterns, and the red points stand for SIFT feature points. Local features are attached to the points, so they can be used to represent local similarity of an image.

We measure the similarity of the two layouts by matching the feature points, as shown in Fig. 6. Let $\boldsymbol{p}$, $\boldsymbol{q}$ be the 128-D feature vector calculated by the SIFT algorithm. D_{th} is the threshold to determine if the two feature points are matched. Therefore, the distance between two feature points (vectors) is defined as

$$d(\boldsymbol{p},\boldsymbol{q}) = \begin{cases} \sqrt{\boldsymbol{p}^\top \boldsymbol{q}}, & \text{if } \sqrt{\boldsymbol{p}^\top \boldsymbol{q}} \le D_{\text{th}} \\ 1, & \text{otherwise} \end{cases} \tag{10}$$

where $\boldsymbol{p}^\top$ is transform of $\boldsymbol{p}$. Equation (10) shows that if the two feature points are close enough, the distance is the Euclidean distance. Otherwise, the distance between them is their L2-Norm which is 1. We set D_{th} to 0.7 in our implementation.

Algorithm 3 shows the similarity calculation between layout w and layout s. For a feature point $\boldsymbol{p}_i^w$ in L_w, we need to find an unmatched point $\boldsymbol{p}_j^s$ in L_s so that the distance $d(\boldsymbol{p}_i^w, \boldsymbol{p}_j^s)$ between them is minimum. If the $d(\boldsymbol{p}_i^w, \boldsymbol{p}_j^s)$ is less than D_{th}, it means the similarity of these two points is high and the pattern distribution near this point is very similar, so we mark them as matched. Fig. 6 shows an example of SIFT matching, where the distance between two matched feature points is stored in D^{ws}. Since the number of feature points differs as the change of layout, the length of D^{ws} after matching points is not the same. If we directly take the D^{ws} as the layout distance, two layouts with more matched feature points tend to have a larger distance, which is opposite to the fact. In order to make all distances comparable, we sort D^{ws} in ascending order, then take the first C additions as the layout distance,

Algorithm 3 Calculate Layout Similarity

Require: Layout L_w and L_s.
Let $\boldsymbol{p}_1^w, \boldsymbol{p}_2^w, ..., \boldsymbol{p}_n^w$ be the feature points in L_w;
Let $\boldsymbol{p}_1^s, \boldsymbol{p}_2^s, ..., \boldsymbol{p}_m^s$ be the feature points in L_s;
Initialize the empty array D^{ws};
for $i = 1 \rightarrow n$ **do**
  for $\boldsymbol{p}_i^w$, find unmatched $\boldsymbol{p}_j^s$ such that $d(\boldsymbol{p}_i^w, \boldsymbol{p}_j^s)$ is minimum;
  if $d(\boldsymbol{p}_i^w, \boldsymbol{p}_j^s) \le D_{th}$ **then**
    mark $\boldsymbol{p}_i^w$, $\boldsymbol{p}_j^s$ matched;
    put $d(\boldsymbol{p}_i^w, \boldsymbol{p}_j^s)$ in D^{ws};
  else
    put 1 in D^{ws};
  end if
end for
sort D^{ws} in an ascending order;
$S_{sift}(L_w, L_s) = \sum_{k=1}^{C} D_k^{ws}$;
return $S_{sift}(L_w, L_s)$;

which is defined as

$$S_{sift}(L_w, L_s) = \sum_{k=1}^{C} D_k^{ws}. \tag{11}$$

In our implementation, C is set to 60.

2) Clustering: Inputting a set of layouts, an adjacency matrix representing the layout distance can be calculated according to (11). Considering the mismatching of feature points will introduce distance noises, which greatly affect the performance of k-means, so we select the k-medoids as the clustering method. The central point of k-means is not a real point in the cluster and is calculated by all points, so noise points also contribute to the movement of central points. But k-medoids chooses real points as the central points, and they are selected by the sum distance in their clusters, therefore, the k-medoids is less sensitive to the noises as you can imagine. The performance of k-medoids is evaluated by the sum of layout distance (SLD), which is given by

$$\text{SLD} = \sum_{i=1}^{M} \sum_{L_k \in C_i} S_{sift}(L_k, L_i) \tag{12}$$

where C_i is a class whose center point is L_i, while L_k is a noncentral point belongs to C_i. There are M classes in total. SLD represents the sum of the distance from each noncentral point to its respective center point. The initial central points are randomly selected. The object is to reduce SLD iteratively by changing the center point and calculating the distance of each class. We set M to 50, and randomly select five layouts in each cluster.

B. Enhanced Layout Sampling

Although with the SIFT distance metric, our framework is able to obtain a fairly good performance which has been verified by our experiments, but due to the limitations of algorithm characteristics, there are still the following challenges.

1) The SIFT distance is based on the matching of similar points. Since SIFT only captures the feature points that are invariant to rotation or scaling, when most parts

Authorized licensed use limited to: The Hong Kong University of Science and Technology (Guangzhou). Downloaded on December 20,2024 at 09:27:14 UTC from IEEE Xplore. Restrictions apply.

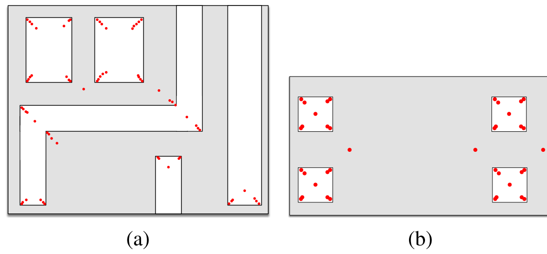

Fig. 7. SIFT feature points distribution. (a) Complex layout. (b) Simple layout.

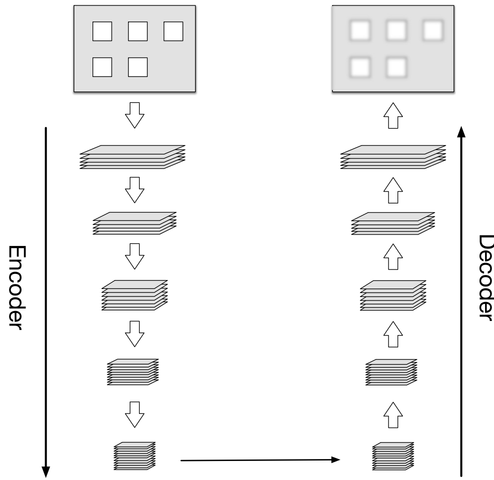

Fig. 8. Autoencoder structure.

of the image are relatively smooth, SIFT may not be able to catch enough feature points. In other words, when extracting the features on a layout composed of simple shapes, a modicum of feature points may cause the degradation of algorithm performance. For example, when matching points and calculating the distance, more feature points in Fig. 7(a) are better to describe the layout than that in Fig. 7(b).

2) Most of the SIFT feature points appear on the corners to detail the shapes. However, there are a lot of repeated shapes in a layout, which not only increases the calculation complexity but also causes over-characterization of a certain area where most of the feature points are distributed. This results in an unbalanced distance measurement among different subareas of a layout.

To address the above issues, we propose an alternative layout distance metric based on autoencoder. Autoencoders are a set of special neural networks used for extracting the latent representation, which contains two components: 1) encoder and 2) decoder. Let $f(\boldsymbol{x})_e$ and $f(\boldsymbol{x})_d$ denote encoder and decoder, respectively, autoencoder is trying to make the input $\boldsymbol{x} \in \mathbb{R}^n$ to be the same as the output, as shown in Fig. 8.

Encoder converts input into latent space expression which can be described as $f(\boldsymbol{x})_e = \boldsymbol{y} \in \mathbb{R}^m$. While decoder reconstructs the input with the process of $f(\boldsymbol{y})_d = \hat{\boldsymbol{x}} \in \mathbb{R}^n$. If we set $m < n$, the training step of the autoencoder forces it to extract the main features of the image. The output $\hat{\boldsymbol{x}}$ is usually a blurred image because encoding is a lossy process that keeps the important image representation in latent space and drops unnecessary information. When training the autoencoder, we

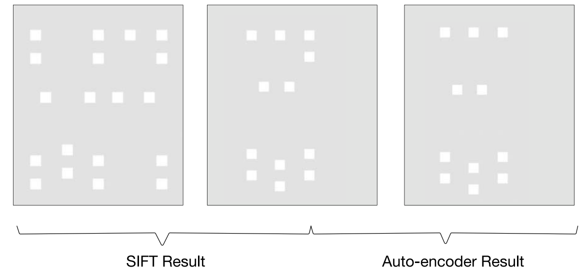

Fig. 9. Clustering result of SIFT-based distance and autoencoder-based distance.

minimize the loss between the original image and the decoder output iteratively to find the best representation. Ideally, each parameter in the latent space $\mathbb{R}^m$ is an independent variable that controls some properties of layout images. Based on above discussions, the layout distance computed from the extracted features is defined as follows:

$$S_{\text{auto}}(L_w, L_s) = \|f(L_w)_e - f(L_s)_e\|_2 \tag{13}$$

where L_w and L_s represent different layouts. The distance between these two layouts is the L_2 norm of encoder output. Based on the distance definition, k-medoids algorithm introduced in Section IV-A can divide them into different clusters. A simple clustering result based on different distance metrics can be seen in Fig. 9. SIFT approach clusters the left and the middle layouts, but the autoencoder approach clusters the middle and the right layouts, which look much more similar. Considering the number of patterns and pattern density differ from each other, the degradation of the SIFT algorithm and the unbalanced measurements of layout may cause the misclassification using the SIFT approach.

The encoder structure resembles ResNet18 [24] with fully connected layers excluded and the decoder uses corresponding deconvolution layers to reconstruct the image. The encoder structure information can be seen in Table II, where “Layer” shows the layer type. Columns “Filter” and “Stride” represent the size of convolution kernels and their strides, and “Output” is the output shape of each layer. The encoder structure is mainly composed of basic blocks. There are two convolutional kernels in a basic block, and batch normalization is added to the end of each convolutional kernel. Each layer contains an identity mapping (it is not shown in the table) to enable the network to go deeper. Each entry in a two-element vector of “Stride” is the corresponding convolution kernel strides of a basic block. From the table, we can see there are $7 \times 7 \times 512 = 25\,088$ parameters to describe a layout, which is about half of the input image size. Table III lists the configurations of the decoder. It is a reversed structure of the encoder, and the deconvolution layer is used for the upsampling process to restore the image. The autoencoder implementation is based on PyTorch [25].

C. Decomposition Sampling

Similar to the problem of layout sampling, although traditional layout decomposition prunes many illegal decomposition results, the remaining decomposition choices still can be very large. The number of decomposition results increases exponentially with the number of patterns as illustrated in

Authorized licensed use limited to: The Hong Kong University of Science and Technology (Guangzhou). Downloaded on December 20,2024 at 09:27:14 UTC from IEEE Xplore. Restrictions apply.

TABLE II
ENCODER STRUCTURE INFORMATION

Layer	Filter	Stride	Output
conv1	7×7×64	2	112×112×64
maxpool	3×3	2	56×56×64
layer1	$\begin{pmatrix} 3\times3\times64 \\ 3\times3\times64 \end{pmatrix}\times 2$	$\begin{pmatrix}1\\1\end{pmatrix} / \begin{pmatrix}1\\1\end{pmatrix}$	56×56×64
layer2	$\begin{pmatrix} 3\times3\times128 \\ 3\times3\times128 \end{pmatrix}\times 2$	$\begin{pmatrix}2\\1\end{pmatrix} / \begin{pmatrix}1\\1\end{pmatrix}$	28×28×128
layer3	$\begin{pmatrix} 3\times3\times256 \\ 3\times3\times256 \end{pmatrix}\times 2$	$\begin{pmatrix}2\\1\end{pmatrix} / \begin{pmatrix}1\\1\end{pmatrix}$	14×14×256
layer4	$\begin{pmatrix} 3\times3\times512 \\ 3\times3\times512 \end{pmatrix}\times 2$	$\begin{pmatrix}2\\1\end{pmatrix} / \begin{pmatrix}1\\1\end{pmatrix}$	7×7×512

TABLE III
DECODER STRUCTURE INFORMATION

Layer	Filter	Stride	Output
deconv1	3×3×256	2	14×14×256
deconv2	3×3×128	2	28×28×128
deconv3	3×3×64	2	56×56×64
deconv4	3×3×64	2	112×112×64
deconv5	7×7×1	2	224×224×1

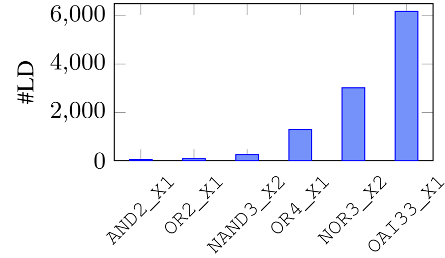

Fig. 10. Growth of decomposition results.

Fig. 10. As the increase of about 9 patterns, the decomposition result size grows from less than 100 to more than 6000. Due to the limitations of computing resources, we are motivated to explore an effective decomposition sampling method. Considering the EPE occurrence is highly related to nearby pattern distribution, the complete combination of patterns in a subregion will be more helpful for our training and n-wise method is able to tackle this problem. In order to focus more promising decomposition solution, we also combine no-odd graph result and n-wise method to generate training set.

Different from the decomposition generation phase in Section III-A, here we divide patterns into two types to reduce the decomposition number, because generating the score of decomposition is much more time-consuming than predicting. According to (14), the patterns $\mathcal{T}$ with the distance d less than $n_{\min}$ are divided into $\mathcal{S}_P$, while the remaining pattern are in $\mathcal{R}_P$ set

$$\mathcal{T} \in \begin{cases} \mathcal{S}_P, & \text{if } d \le n_{\min} \\ \mathcal{R}_P, & \text{if } n_{\min} < d \end{cases} \tag{14}$$

where $n_{\min}$ is set to 80 nm, that is same to the configuration in Section III-A.

Similar to generating *mergedArrs*1 in Section III-A, we first divide patterns into two types, $\mathcal{S}_P$ and $\mathcal{R}_P$. By solving nonodd graph problem, we can obtain the relative position relationship of $\mathcal{S}_P$, then we build the three-wise arrays together with $\mathcal{R}_P$. Finally, we reverse the value and merge the same rows. In our implementation, generating three-wise arrays is a tradeoff between prediction accuracy and layout score simulation running time. Three-wise sampling strategy ensures that the training set contains the complete combination of any subregion with three patterns (part of patterns in $\mathcal{S}_P$ are excluded).

D. Model Training

To avoid the dual layout problem, the input will be formatted as mentioned in Section III-A. In this article, L_2 error and EPE numbers are selected as the evaluation metrics. Since the occurrences of print violations will lead to a significant decline in printability, the score of decomposition is organized as follows:

$$\text{score} = \alpha \times \#L_2 \text{ Error} + \beta \times \#\text{EPE} + \gamma \times \#\text{Violation}. \tag{15}$$

In our implementation, α, β, and γ are 1, 3500, and 8000, respectively, and z-score regularization is applied which is given by

$$z\text{-score} = \frac{\text{score}_i - \mu}{\sigma} \tag{16}$$

where score_i is the ith layout score we defined in (15), μ is the mean of decomposition results, and σ is the standard deviation. It describes how many standard deviations the score is from the mean, and data are converted into the same magnitude to ensure the comparability between the data. We use z-score as the decomposition quality. The mean absolute error (MAE) is applied as the cost function

$$\text{MAE} = \frac{\sum_{i=1}^{n} |y_i - \hat{y}_i|}{n} \tag{17}$$

where y_i denotes the label of the ith decomposition in the training set, and $\hat{y}_i$ is the corresponding predicted value.

The image dimension is 224 × 224, which increases the complexity of training. Here, Adam optimizer [29] is selected to train the model. Compared to the mini-batch gradient, Adam computes individual adaptive learning rates for different parameters which is more suitable for large-scale data.

We also take the structure of ResNet18 as the basic regression network (see Fig. 11). It is similar to the encoder structure, and details of convolutional layers can be seen in Table II. The network implementation is based on PyTorch [25] library. The identity mapping in each basic block enables the net layer to become deeper to obtain a better regression of object function. The input of the net is 224 × 224 × 1 tensor to receive a grayscale image, and the output of stacked conventional layers is 7 × 7 × 512 cube. After average pooling, there is a 1000 dimensions layer, and a fully connected layer is added to output the score.

Authorized licensed use limited to: The Hong Kong University of Science and Technology (Guangzhou). Downloaded on December 20,2024 at 09:27:14 UTC from IEEE Xplore. Restrictions apply.

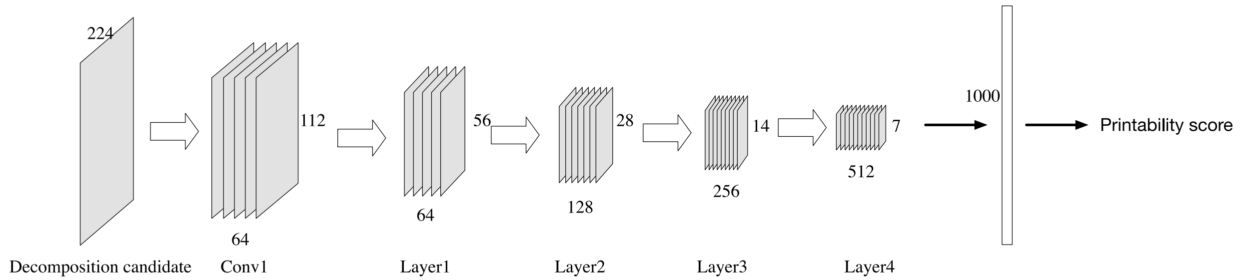

Fig. 11. Printability predictor structure.

TABLE IV
COMPARISON WITH PREVIOUS FRAMEWORKS

ID	[26] + [5]		[27] + [5]		[9]		SIFT distance [28]		Ours-Balanced		Ours	
	EPE #	Time (s)	EPE #	Time (s)	EPE #	Time (s)	EPE #	Time (s)	EPE #	Time (s)	EPE #	Time (s)
INV_X1	1	1183	1	1183	1	1995	0	169	0	182	0	181
NOR2_X1	8	1421	4	1405	1	1996	1	208	0	191	0	278
BUF_X1	5	867	5	1068	1	1990	0	228	2	298	0	170
CLKBUF_X1	1	1046	1	737	0	1996	0	176	0	170	0	200
OAI211_X1	5	1213	7	1207	6	1996	0	217	2	302	1	196
AOI211_X1	5	1048	8	1080	1	1989	2	295	0	297	0	292
AND2_X1	13	1080	13	1061	1	1993	0	273	0	182	1	282
OR2_X1	7	1046	3	1220	0	1997	1	234	0	234	1	281
NAND4_X1	5	1173	6	1176	1	1997	1	241	0	200	0	178
NAND3_X2	7	1171	8	774	3	1998	0	303	1	281	0	194
OR4_X1	5	1188	2	1233	0	1987	1	229	2	289	0	205
NOR3_X2	5	773	4	1168	7	1999	4	299	1	297	1	357
OAI33_X1	11	1017	10	922	6	1998	0	272	1	299	1	294
Average	6.00	1094.31	5.53	1094.92	2.15	1994.69	0.76	241.84	0.69	247.80	0.39	239.10
Ratio	15.39	4.58	14.18	4.58	5.51	8.34	1.94	1.01	1.77	1.03	**1.00**	**1.00**

V. EXPERIMENTAL RESULT

The proposed framework is implemented in C++ and validations are performed on Intel i7 3.6-GHz CPU. The printability estimation network and autoencoder are implemented in PyTorch [25]. To generate n-wise sampling arrays, we use PICT [30], an open source C library. The open source lithography simulator and EPE checker are from [19]. The EPE violation threshold is set to 10 nm and the approximated optical model kernel number K is set to 24. Experiments are conducted on an open source cell library NanGate [31]. The layout dataset is generated using [32], which takes a set of design rules for contact layer and yields in total 8000 designs. These designs resemble NanGate 45 nm library and are verified with Mentor Calibre design rule check.

A. Framework Evaluation

In the first experiment, we compare the optimization result of our framework with previous unified framework and two-stage independent flow on standard cell library NanGate, as shown in Table IV. We obtain binary from the authors of [9], and the results of the two other conventional flows are directly from [9]. Columns "EPE" and "Time (s)" list the number of EPE violations and the time elapsed in seconds when the optimization is convergent. Column "Ours" lists the results of our deep learning-based framework without applying density balance (in Section III-B), while column "Ours-Balanced" lists the results with the density balance checking. Compared with previous work [28], our frameworks ("Ours" and "Ours-Balanced") use autoencoder as distance metric.

In Table IV, our frameworks show significant improvement in "EPE" and "Time" on average. The runtime of "Ours" is 239.10 s, which achieves around 4× speed-up compared with [26]+[5] and [27]+[5], and 8× speed-up compared to "[9]." That is because our framework does not need to get the decomposition by solving the SDP problem [9] and select decomposition candidates by lithography simulation, both of which are extremely time consuming.

In terms of "EPE," "Ours" approach reduced five EPE violations compared with [28] in total. The EPE violation performance between [28] and "Ours" is very similar in most cases, except for NOR3_X2 test case (four EPE violations versus one EPE violation). One possible reason why [28] results in a greater number of EPE violations (four EPE violations in cell NOR3_X2) is that the pattern distribution of this layout is unfriendly for ILT optimization. But it is encouraging to see the training set of "Ours" reaches better coverage of layout data, so it can handle this kind of layout distribution well. Our framework reduced 81.9% EPE violations compared to [9] and 92.9% EPE violations compared to two conventional flows (i.e., [26]+[5] and [27]+[5]). Besides, we can observe that applying density balance checking ("Ours-Balanced") results in more EPE violations compared with "Ours." One possible reason is that the decomposition predictor is trained with imbalanced decomposition, as we want the predictor to learn all kinds of data such that it becomes a more general model.

There are some examples of optimization results in Fig. 12. The EPE violations are marked as red crosses in the image. It can be seen that both of SIFT approach and autoencoder approach have fewer EPE violations and better printability on contact layers of the standard cells.

Authorized licensed use limited to: The Hong Kong University of Science and Technology (Guangzhou). Downloaded on December 20,2024 at 09:27:14 UTC from IEEE Xplore. Restrictions apply.

Fig. 12. Comparison with ICCAD'17 [9] and DAC'20 [28] on: (a) BUF_X1; (b) OAI211_X1; (c) NAND3_X2. (d) NOR3_X2. (e) OAI33_X1. Compared with the state of the art, in all five cases, our framework results in fewer EPEs.

B. Sampling Strategy Evaluation

To demonstrate the efficiency of our sampling strategy, we compare the EPE number of the random sampling approach and the proposed approach. As shown in Fig. 13, "SIFT distance" and "Autoencoder distance" are trained in the way we introduced in Section IV. "Random Sampling" is trained in the same way but the training set is randomly sampled from generated layouts and layout decompositions are randomly generated from the corresponding sampled layouts. Although these layouts and decompositions in "Random" are randomly sampled, the decomposition generation module still offers legal decomposition results to the estimation module.

It can be observed in the bar chart that the EPE number of "Random sampling" strategy is more than three times of "Autoencoder distance" strategy and twice of "SIFT distance" strategy. Since random sampling layouts can hardly find promising results in solution space, the training set distribution should obey the distribution of generated layouts. As a result, random sampling quality is determined, to some extent, by the quality of distribution of the generated layout database, which may not promise a reasonable layout sampling result.

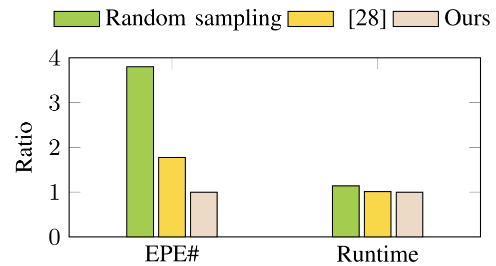

Fig. 13. Comparison with random sampling strategy.

For a specific layout, the solution space is too large, but many of the results can be discarded by formulating some physical rules, so random sampling needs to sample more decompositions to fill the gap. Our sampling strategy focuses on the possible decomposition while the random sampling is equivalent to sampling evenly at the solution space, which needs much more training data. An example of a printed image optimized by the three different estimation models is illustrated in Fig. 14.

Authorized licensed use limited to: The Hong Kong University of Science and Technology (Guangzhou). Downloaded on December 20,2024 at 09:27:14 UTC from IEEE Xplore. Restrictions apply.

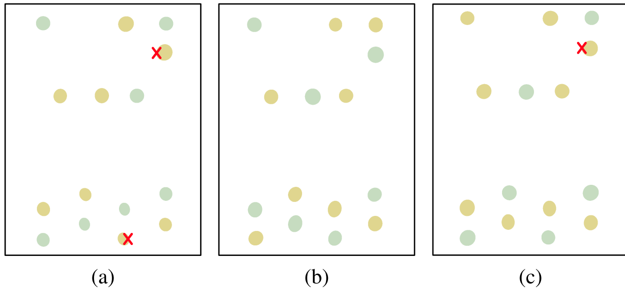

Fig. 14. Comparison of different approaches on AND2_X1. (a) Result of random sampling with 2 EPE violations. (b) Result of SIFT distance model with 0 EPE violation. (c) Result of autoencoder distance model (w/o. density balance) with 1 EPE violation.

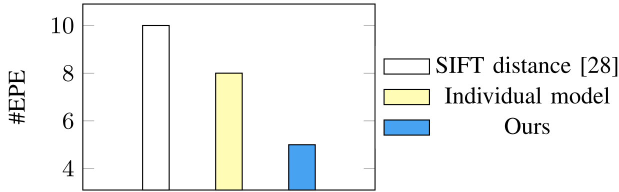

Fig. 15. Comparison with the simplified estimation model.

C. Individual Printability Estimation

In the LELE-type lithography setting, the printability can be estimated independently, through which two decomposed mask scores can be estimated individually and summed up. In the training stage, we can generate decomposition candidates as two images. The forward optimization flow is the same as our framework, shown in the left part of Fig. 2, except for the printability prediction module. The new estimation model has two advantages.

1) It is a more flexible method, as a well-trained model can be extended to triple mask patterning technology and beyond without retraining the model.
2) This kind of model will not meet the dual problem represented as Fig. 4, so it is an easier way to process data.

We implemented this model and conducted the experiments, and the corresponding results are shown in Fig. 15. The new estimation model is represented with yellow color, while "Ours" is the approach introduced in Section III. From the result we can observe that the "Simplified model" shows a good result with eight EPE violations, which is fewer than [28], but still has three more EPE violations than "Ours."

D. Handling Large-Scale Chips

The proposed method is verified on standard cells, and it is possible to extend our framework to the layouts of large circuits. In order to show the scalability of our framework, we conducted the experiment on a large circuit (10840 nm $\times$7890 nm) synthesized using the same NanGate [31] library as used in previous experiments. The layout is divided into 22 clips using a sliding window-based method with overlap, in which some empty and duplicated clips are ignored in the result. The results are shown in Table V. We implemented the decomposition generation and selection method of LDMO [9] as the baseline, the results are listed in the "LDMO [9]" column of Table V. "Ours" is the introduced

TABLE V
COMPARISON ON LARGE CIRCUIT DESIGN

ID	LDMO [9]		Ours	
	EPE#	Time (s)	EPE#	Time (s)
CLIP0	2	766	3	293
CLIP1	8	785	6	300
CLIP2	3	743	2	289
CLIP3	2	759	2	282
CLIP4	5	901	3	299
CLIP5	10	712	7	289
CLIP6	2	704	1	285
CLIP7	2	774	1	290
CLIP8	3	1015	3	283
CLIP9	4	922	0	261
CLIP10	7	1080	7	322
CLIP11	3	729	1	301
CLIP12	3	724	3	295
CLIP13	0	620	0	194
CLIP14	0	660	0	209
CLIP15	1	706	1	279
CLIP16	0	744	0	276
CLIP17	0	601	1	276
CLIP18	0	668	0	249
CLIP19	1	709	0	222
CLIP20	3	707	5	298
CLIP21	0	643	0	213
Average	2.68	757.81	2.09	272.95
Ratio	1.28	2.78	**1.00**	**1.00**

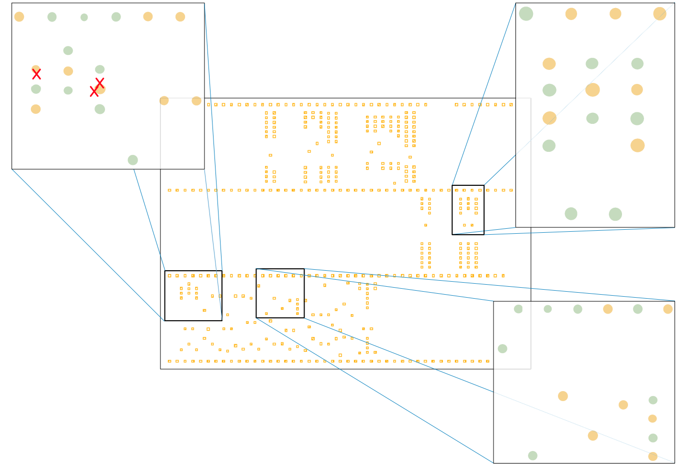

Fig. 16. Large circuit design and clip optimization examples.

framework without applying density balance checking. The average EPE violations of "Ours" are 2.09, while "LDMO [9]" outputs 2.68. Although very dense or very sparse pattern distributions may lead to the degradation of our decomposition generation, "Ours" still reduces 22% EPE violations and takes only 36% runtime compared to the baseline. The printability prediction module shows its effectiveness and efficiency when handling divergent layouts. The large circuit design and some clip optimization results are illustrated in Fig. 16.

VI. DISCUSSION

A. Adopting ML-Based Lithography Simulation

In addition to the machine learning (ML)-based printability prediction method we used in our framework, ML-based lithography simulation methods [33], [34] are also widely applied. The main differences are that, given some masks, ML-based printability prediction tells if the

Authorized licensed use limited to: The Hong Kong University of Science and Technology (Guangzhou). Downloaded on December 20,2024 at 09:27:14 UTC from IEEE Xplore. Restrictions apply.

masks/decomposition candidates are OPC-friendly through inferring some concrete evaluation metrics (e.g., EPE# and L2 error in this work). While ML-based lithography simulation outputs the printed shapes, which can be used to infer the performance on different metrics. It usually faces a much larger solution space. But please note that it cannot estimate the printability after many iterations of OPC, as this kind of model just accelerates the lithography simulation process, and the output changes with the reshaping of masks. In general, the two methods focus on different points and can be applied for different purposes.

In our framework, obtaining the optimal MO result can be divided into two steps: 1) finding the best decomposition and 2) conducting ILT for this pair of masks. In order to find the best decomposition, we applied the ML-based printability prediction method. As for the subsequent ILT process, ML-based lithography simulation can be chosen as an acceleration method.

B. Handling More Masks

The related modules for applying more advanced MPL are decomposition generation module and ILT optimization module. For decomposition generation module, it mainly involves two processes: 1) building the no-odd graph and 2) applying n-wise method. In the scenario of triple patterning lithography, decomposition generation module solves three-coloring problems, where assigning different colors to the neighbor in no-odd graph cannot handle. But methods for triple patterning decomposition have been well investigated [1]–[4]. By adopting [3], we can solve the conflicts among violated patterns. As for n-wise method, it is suitable for the three-coloring problem because it can tackle a factor with three levels, where each level can be viewed as a color. Then applying (three-level) n-wise method to generate arrays and combining the results, we are able to obtain three-color decomposition candidates.

For ILT optimization module, we can observe from (4) and (5) that the optimization formulations are not limited to the mask number. Therefore, it can be easily extended by introducing a new mask variable $\boldsymbol{M}_3$. After applying the sigmoid transformation to $\boldsymbol{M}_3$, ILT is able to minimize the L_2 error, thus our framework can handle more advanced MPL.

C. Extend to Other Layers

Our framework is developed based on contact layers, but it has the potential to be extended to metal layers. Since the printability prediction module is not limited by a particular layer, the prediction model still can supervise the layout decomposition process and is expected to achieve excellent performance on other layers with sufficient training data. As for the decomposition generation module, a much denser conflict graph may cause the degradation on decomposition generation performance and stitch insertion problems need to be handled. Therefore, more general decomposition algorithms [1]–[4] that take stitch insertion into consideration, need to be applied for obtaining more proper decomposed masks.

VII. Conclusion

In this article, we propose a deep learning-driven framework to not just bridge the gap between LDMO but also speed up the procedure of selecting decomposition process. To improve the prediction accuracy and accelerate the training process, we use SIFT and autoencoder to extract layout features. K-medoids clustering and n-wise method are adopted to generate the training set. We also combine the no-odd graph and n-wise method to generate decomposition candidates with different pattern combination strengths. Experiments demonstrate that our framework can efficiently reduce EPE violations and accelerate the overall optimization process.

References

[1] J. Kuang and E. F. Y. Young, "An efficient layout decomposition approach for triple patterning lithography," in *Proc. ACM/IEEE Design Autom. Conf. (DAC)*, 2013, p. 69, doi: 10.1145/2463209.2488818.

[2] H.-Y. Chang and I. H.-R. Jiang, "Multiple patterning layout decomposition considering complex coloring rules," in *Proc. ACM/IEEE Design Autom. Conf. (DAC)*, 2016, p. 40, doi: 10.1145/2897937.2898048.

[3] B. Yu, K. Yuan, D. Ding, and D. Z. Pan, "Layout decomposition for triple patterning lithography," *IEEE Trans. Comput.-Aided Design Integr. Circuits Syst.*, vol. 34, no. 3, pp. 433–446, Mar. 2015, doi: 10.1109/TCAD.2014.2387840.

[4] S.-Y. Fang, Y.-W. Chang, and W.-Y. Chen, "A novel layout decomposition algorithm for triple patterning lithography," *IEEE Trans. Comput.-Aided Design Integr. Circuits Syst.*, vol. 33, no. 3, pp. 397–408, Mar. 2014, doi: 10.1145/2228360.2228579.

[5] J.-R. Gao, X. Xu, B. Yu, and D. Z. Pan, "MOSAIC: Mask optimizing solution with process window aware inverse correction," in *Proc. ACM/IEEE Design Autom. Conf. (DAC)*, 2014, p. 52, doi: 10.1145/2593069.2593163.

[6] A. Poonawala and P. Milanfar, "Mask design for optical microlithography—An inverse imaging problem," *IEEE Trans. Image Process.*, vol. 16, no. 3, pp. 774–788, Mar. 2007, doi: 10.1109/TIP.2006.891332.

[7] N. Jia and E. Y. Lam, "Machine learning for inverse lithography: Using stochastic gradient descent for robust photomask synthesis," *J. Opt.*, vol. 12, no. 4, 2010, Art. no. 045601, doi: 10.1088/2040-8978/12/4/045601.

[8] H. Yang, S. Li, Z. Deng, Y. Ma, B. Yu, and E. F. Y. Young, "GAN-OPC: Mask optimization with lithography-guided generative adversarial nets," *IEEE Trans. Comput.-Aided Design Integr. Circuits Syst.*, vol. 39, no. 10, pp. 2822–2834, Oct. 2020, doi: 10.1109/tcad.2019.2939329.

[9] Y. Ma, J.-R. Gao, J. Kuang, J. Miao, and B. Yu, "A unified framework for simultaneous layout decomposition and mask optimization," in *Proc. IEEE/ACM Int. Conf. Computer-Aided Design (ICCAD)*, 2017, pp. 81–88, doi: 10.1109/iccad.2017.8203763.

[10] Z. Xie *et al.*, "RouteNet: Routability prediction for mixed-size designs using convolutional neural network," in *Proc. IEEE/ACM Int. Conf. Comput.-Aided Design (ICCAD)*, 2018, p. 80, doi: 10.1145/3240765.3240843.

[11] H. Yang, J. Su, Y. Zou, Y. Ma, B. Yu, and E. F. Y. Young, "Layout hotspot detection with feature tensor generation and deep biased learning," *IEEE Trans. Comput.-Aided Design Integr. Circuits Syst.*, vol. 38, no. 6, pp. 1175–1187, Jun. 2019, doi: 10.1109/TCAD.2018.2837078.

[12] Y. Lin *et al.*, "Data efficient lithography modeling with residual neural networks and transfer learning," in *Proc. ACM Int. Symp. Phys. Design (ISPD)*, 2018, pp. 82–89, doi: 10.1145/3177540.3178242.

[13] D. G. Lowe, "Object recognition from local scale-invariant features," in *Proc. 7th IEEE Int. Conf. Comput. Vis.*, vol. 2, 1999, pp. 1150–1157, doi: 10.1109/ICCV.1999.790410.

[14] C. Geng and X. Jiang, "Face recognition using sift features," in *Proc. 16th IEEE Int. Conf. Image Process. (ICIP)*, 2009, pp. 3313–3316, doi: 10.1109/ICIP.2009.5413956.

[15] H. Huang, W. Guo, and Y. Zhang, "Detection of copy-move forgery in digital images using sift algorithm," in *Proc. IEEE Pac. Asia Workshop Comput. Intell. Ind. Appl.*, vol. 2. 2008, pp. 272–276, doi: 10.1109/PACIIA.2008.240.

[16] H. H. Hopkins, "The concept of partial coherence in optics," *Proc. Royal Soc. London A, Math. Phys. Eng. Sci.*, vol. 208, no. 1093, pp. 263–277, 1951, doi: 10.1098/rspa.1951.0158.

[17] N. B. Cobb, "Fast optical and process proximity correction algorithms for integrated circuit manufacturing," Ph.D. dissertation, Dept. Electr. Eng. Comput. Sci., Univ. California, Berkeley, CA, USA, 1998.

[18] X. Zhao and C. Chu, "Line search-based inverse lithography technique for mask design," *VLSI Design*, 2012, doi: 10.1155/2012/589128.

Authorized licensed use limited to: The Hong Kong University of Science and Technology (Guangzhou). Downloaded on December 20,2024 at 09:27:14 UTC from IEEE Xplore. Restrictions apply.

[19] S. Banerjee, Z. Li, and S. R. Nassif, "ICCAD-2013 CAD contest in mask optimization and benchmark suite," in *Proc. IEEE/ACM Int. Conf. Comput.-Aided Design (ICCAD)*, 2013, pp. 271–274, doi: 10.1109/ICCAD.2013.6691131.
[20] R. Mandl, "Orthogonal latin squares: An application of experiment design to compiler testing," *Commun. ACM*, vol. 28, no. 10, pp. 1054–1058, 1985, doi: 10.1145/4372.4375.
[21] N. Ma, "Automatic IC hotspot classification and detection using pattern-based clustering," Ph.D. dissertation, Dept. Mech. Eng., Univ. California, Berkeley, CA, USA, 2008.
[22] W.-Y. Wen, J.-C. Li, S.-Y. Lin, J.-Y. Chen, and S.-C. Chang, "A fuzzy-matching model with grid reduction for lithography hotspot detection," *IEEE Trans. Comput.-Aided Design Integr. Circuits Syst.*, vol. 33, no. 11, pp. 1671–1680, Nov. 2014, doi: 10.1109/TCAD.2014.2351273.
[23] H. Yao, S. Sinha, C. Chiang, X. Hong, and Y. Cai, "Efficient process-hotspot detection using range pattern matching," in *Proc. IEEE/ACM Int. Conf. Comput.-Aided Design (ICCAD)*, 2006, pp. 625–632, doi: 10.1145/1233501.1233630.
[24] K. He, X. Zhang, S. Ren, and J. Sun, "Deep residual learning for image recognition," in *Proc. IEEE Conf. Comput. Vis. Pattern Recognit. (CVPR)*, 2016, pp. 770–778, doi: 10.1109/CVPR.2016.90.
[25] A. Paszke *et al.*, "PyTorch: An imperative style, high-performance deep learning library," in *Proc. Conf. Neural Inf. Process. Syst. (NIPS)*, 2019, pp. 8024–8035.
[26] Z. Chen, H. Yao, and Y. Cai, "SUALD: Spacing uniformity-aware layout decomposition in triple patterning lithography," in *Proc. IEEE Int. Symp. Qual. Electron. Design (ISQED)*, 2013, pp. 566–571, doi: 10.1109/ISQED.2013.6523667.
[27] B. Yu and D. Z. Pan, "Layout decomposition for quadruple patterning lithography and beyond," in *Proc. ACM/IEEE Design Autom. Conf. (DAC)*, 2014, p. 53, doi: 10.1145/2593069.2593152.
[28] W. Zhong, S. Hu, Y. Ma, H. Yang, X. Ma, and B. Yu, "Deep learning-driven simultaneous layout decomposition and mask optimization," in *Proc. ACM/IEEE Design Autom. Conf. (DAC)*, 2020, pp. 1–6.
[29] D. P. Kingma and J. Ba, "Adam: A method for stochastic optimization," in *Proc. Int. Conf. Learn. Represent. (ICLR)*, 2015, p. 13.
[30] Microsoft Corporation. *Pairwise Independent Combinatorial Testing*. Accessed: Oct. 3, 2019. [Online]. Available: https://github.com/microsoft/pict
[31] (2008). *NanGate FreePDK45 Generic Open Cell Library*. [Online]. Available: http://www.si2.org/openeda.si2.org/projects/nangatelib
[32] H. Yang, W. Chen, P. Pathak, F. Gennari, Y.-C. Lai, and B. Yu, "Automatic layout generation with applications in machine learning engine evaluation," 2019. [Online]. Available: arXiv:1912.05796. doi: 10.1109/mlcad48534.2019.9142121.
[33] B. Jiang, H. Zhang, J. Yang, and E. F. Young, "A fast machine learning-based mask printability predictor for OPC acceleration," in *Proc. IEEE/ACM Asia South Pac. Design Autom. Conf. (ASPDAC)*, 2019, pp. 412–419, doi: 10.1145/3287624.3287682.
[34] W. Ye, M. B. Alawieh, Y. Lin, and D. Z. Pan, "LithoGAN: End-to-end lithography modeling with generative adversarial networks," in *Proc. ACM/IEEE Design Autom. Conf. (DAC)*, 2019, p. 107, doi: 10.1145/3316781.3317852.

Wei Zhong received the B.S. degree from the Dalian University of Technology, Dalian, China, in 2008, and the M.S. and Ph.D. degrees from Waseda University, Tokyo, Japan, in 2010 and 2014, respectively.

He served as a Research Assistant with the Information, Production and Systems Research Center, Waseda University, Kitakyushu, Japan, from 2010 to 2011, an Associate Specialist with the Central Research Laboratory, Ricoh Company, Tokyo, from 2011 to 2014, a Chief Designer and the Director of the Institute of Image Processing Technology, State Key Laboratory of Digital Multimedia Technology, Hisense Group, Qingdao, China, from 2014 to 2018. From 2015 to 2017, he also served as a Postdoctoral Researcher with the University of Science and Technology of China, Hefei, China. He is currently an Associate Professor with the International School of Information Science and Engineering, Dalian University of Technology. His research interests include several aspects of computer vision and image processing algorithms, VLSI design automation, networks on chips, and hardware–software co-design of embedded systems.

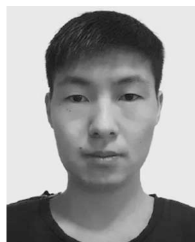

Shuxiang Hu received the B.E. degree from the Department of Software, Hefei University of Technology, Hefei, China. He is currently pursuing the M.S. degree with the International School of Information Science and Engineering, Dalian University of Technology, Dalian, China.

His research interests include VLSI automation and deep learning on chips.

Yuzhe Ma (Member, IEEE) received the B.E. degree from the Department of Microelectronics, Sun Yat-sen University, Guangzhou, China, in 2016, and the Ph.D. degree from the Department of Computer Science and Engineering, Chinese University of Hong Kong, Hong Kong, in 2020.

He has interned with Cadence Design Systems, San Jose, CA, USA, NVIDIA Research, Austin, TX, USA, and Tencent Youtu X-Lab, Shenzhen, China. His research interests include VLSI design for manufacturing, physical design, and machine learning on chips.

Dr. Ma received the Best Paper Award from ASPDAC'2021, the Best Student Paper Award from ICTAI'2019, the Best Paper Award Nomination from ASPDAC'2019, and the Best Poster Research Award from Student Research Forum of ASPDAC'2020.

Haoyu Yang received the B.E. degree from Qiushi Honors College, Tianjin University, Tianjin, China, in 2015, and the Ph.D. degree from the Department of Computer Science and Engineering, Chinese University of Hong Kong (CUHK), Hong Kong, in 2020.

He is currently working as a Postdoctoral Fellow with the Department of Computer Science and Engineering, CUHK. He has interned with ASML, San Jose, CA, USA, and Cadence Design Systems, San Jose. His research interests include machine learning in VLSI design for manufacturability, high performance VLSI physical design with parallel computing, and machine learning security.

Dr. Yang received the Nick Cobb Scholarship from SPIE'2019 Advanced Lithography, the Best Paper Award Nomination from ASPDAC'2019, and the Best Poster Presentation from Student Research Forum of ASPDAC'2019.

Xiuyuan Ma received the B.E. degree from the Dalian University of Technology, Dalian, China, in 2020, where she is currently pursuing the master's degree.

His research interests include machine learning and edge computing.

Bei Yu (Member, IEEE) received the Ph.D. degree from the University of Texas at Austin, Austin, TX, USA, in 2014.

He is currently an Assistant Professor with the Department of Computer Science and Engineering, Chinese University of Hong Kong, Hong Kong.

Dr. Yu received the seven Best Paper Awards from ASPDAC 2021, ICTAI 2019, Integration, the VLSI Journal in 2018, ISPD 2017, SPIE Advanced Lithography Conference 2016, ICCAD 2013, and ASPDAC 2012, and six ICCAD/ISPD contest awards. He has served as a TPC Chair of ACM/IEEE Workshop on Machine Learning for CAD, and in many journal editorial boards and conference committees. He is an Editor of IEEE TCCPS Newsletter.

Authorized licensed use limited to: The Hong Kong University of Science and Technology (Guangzhou). Downloaded on December 20,2024 at 09:27:14 UTC from IEEE Xplore. Restrictions apply.